Acta Materialia 296 (2025) 121231

Contents lists available at ScienceDirect

Acta Materialia

journal homepage: www.elsevier.com/locate/actamat

Full length article

# Strong hydrogen trapping by tangled dislocations in cold-drawn pearlitic steels

Chao Huang [a,b,1], Chuanjie Cui [c,1], Ranming Niu [a,b,1,*], Fenghua Lu [d], Cheng-Yun Wu [a,e], Xiaoxiong Zhu [f], Hongzhou Lu [g], Yongqing Zhang [g], Pang-Yu Liu [a,b], Bosheng Dong [a,b], Yi-Hsuan Sun [a,h], Hongjian Wang [b], Wei Li [d], Hung-Wei Yen [h,i], Aimin Guo [g], Julie M. Cairney [a,b,*], Emilio Martínez-Pañeda [c,*], Eason Yi-Sheng Chen [a,j,*]

[a] Australian Centre for Microscopy and Microanalysis, The University of Sydney, Sydney, NSW, 2006, Australia
[b] School of Aerospace, Mechanical and Mechatronic Engineering, The University of Sydney, Sydney, NSW, 2006, Australia
[c] Department of Engineering Science, The University of Oxford, Oxford, OX1 3PJ, United Kingdom
[d] School of Materials Science and Engineering, Shanghai Jiao Tong University, Shanghai, 200240, China
[e] School of Biomedical Engineering, The University of Sydney, Sydney, NSW, 2006, Australia
[f] Jiangsu Tokyo Rope Co., Ltd., Jiangyin, Jiangsu, 214445, China
[g] CITIC Metal Co., Beijing, 100004, China
[h] Department of Materials Science and Engineering, National Taiwan University, Taipei, 10617, Taiwan
[i] Advanced Research Center for Green Materials Science and Technology, National Taiwan University, Taipei, 10617, Taiwan
[j] School of Materials Science and Engineering, Nanyang Technological University, Singapore, 639798, Singapore

ARTICLE INFO

*Key words:*
Hydrogen embrittlement
Hydrogen trapping
Steels
Atom probe tomography
Materials design

ABSTRACT

The presence of diffusible hydrogen atoms can lead to hydrogen embrittlement in steels, compromising their structural integrity. A potential solution is incorporating strong hydrogen traps into the microstructures to immobilize hydrogen solute atoms and prevent their diffusion towards stress-prone areas where embrittlement is most likely to occur. However, creating materials with effective hydrogen traps usually involves adding expensive alloying elements, which increase the production costs, hindering the adoption of this strategy in the steel industry. Here we show that cold drawing of pearlitic steel rods introduces a high density of dislocations that accumulate and tangle at cementite-ferrite interfaces; this strengthens the steel and make it less susceptible to embrittlement. We use atom probe tomography to confirm that these tangled dislocations firmly trap hydrogen in a steel that displays low embrittlement susceptibility. Our findings suggest a pathway for producing metallic materials that have an excellent combination of high strength and hydrogen embrittlement resistance, underscoring the potential of using structural defects as cost-effective hydrogen traps.

## 1. Introduction

The absorption of hydrogen in structural metals can significantly reduce their toughness, a phenomenon known as hydrogen embrittlement [1–4]. This issue poses serious risks for the transportation and storage of hydrogen, a carbon-free fuel, in steel-based gas handling systems [2,3]. Various government white papers have highlighted the issue of increased maintenance costs and weakened material properties due to hydrogen embrittlement in gas infrastructure [5–7]. Given the high flammability of hydrogen, material failures and resulting gas leaks could delay progress towards a hydrogen-based economy for decarbonization. This would undermine hydrogen's advantages as a clean energy source that addresses the intermittency of solar and wind power. Hydrogen embrittlement also presents a major challenge in the automotive industry, where there is a desire to use stronger steels to reduce vehicle weight for fuel efficiency, but these high strength materials are more susceptible to hydrogen embrittlement [3,8].

To reduce the risk of embrittlement in metals, it is crucial to

* Corresponding authors.
*E-mail addresses:* ranming.niu@sydney.edu.au (R. Niu), julie.cairney@sydey.edu.au (J.M. Cairney), emilio.martinez-paneda@eng.ox.ac.uk (E. Martínez-Pañeda), eason.chen@ntu.edu.sg (E.Y.-S. Chen).
[1] The authors contributed equally to this work.

https://doi.org/10.1016/j.actamat.2025.121231
Received 15 March 2025; Received in revised form 4 June 2025; Accepted 7 June 2025
Available online 7 June 2025

minimize hydrogen absorption during the production of metal components [3,9]. One approach is controlling the dew point during heat treatment, which limits exposure to moisture [3]. Another common method is post-production baking, which removes absorbed hydrogen from the metal [3]. Surface coatings can also be applied to slow hydrogen uptake, delaying the time it takes for the metal to reach the critical hydrogen content that leads to embrittlement [2,3,10]. Once hydrogen enters the metallic structure, microstructural hydrogen traps can reduce the amount of freely diffusing hydrogen, reducing its availability to facilitate crack initiation and propagation and ultimately cause embrittlement [3,9,11].

The effectiveness of hydrogen traps for embrittlement mitigation depends on their ability to retain hydrogen at operational temperatures for long periods [3,9,11]. Despite decades of research into hydrogen trapping as a solution to embrittlement [12–14], its overall effectiveness is still in debate. Early theoretical work argues that trapped hydrogen may create a "local equilibrium" with the surrounding matrix that has a lower hydrogen concentration [14,15]. This local equilibrium can result in the release of trapped hydrogen to the matrix and subsequently to either the surrounding environment or regions with lower hydrogen concentration. Even very strong traps, e.g., binding energies higher than 70 kJ/mol [3,9], are expected to quickly release hydrogen in a desorbing metal. However, this local equilibrium theory has not been experimentally proven, particularly regarding whether microstructural traps exist that can firmly hold hydrogen for long durations [11,13,14,16,17]. This uncertainty undermines confidence in the use of hydrogen trapping as a material design criterion to achieve embrittlement resistance in industrial alloys, alongside other important factors such as toughness, heat resistance, and cost-effectiveness.

To experimentally study hydrogen trapping, thermal desorption spectroscopy (TDS) has traditionally been used [3,18]. TDS measures the total hydrogen released from materials, including the contributions from any incorporated traps. However, it does not provide information about which specific microstructures are responsible for trapping the hydrogen. Although transmission electron microscopy (TEM) has been used to complement TDS data by providing microstructural details [3,19], linking hydrogen desorption peaks to specific microstructures remains speculative. In addition, TDS has also been used to estimate how firmly hydrogen is trapped, i.e., trapping/detrapping energies, but these estimates rely on a simplified one-step hydrogen detrapping model, mainly developed by Kissinger [20], which assumes that hydrogen escapes from a trap and desorbs instantly without interacting with other nearby microstructural traps. Uncertainties in the role of specific trap types also limit the ability to utilize traps in materials design for embrittlement resistance.

In recent years, atom probe tomography (APT) has been used to directly observe hydrogen trapping in specific microstructures [21,22]. APT combines high sensitivity for hydrogen detection with spatial resolution, allowing researchers to study the hydrogen localization at specific microstructures of interest, such as dislocations [23,24], grain boundaries [23,25], and carbide precipitates [23,26–29]. APT experiments often use deuterium ($^2$H or D), a hydrogen isotope, to distinguish between hydrogen present in the sample and background noise caused by residual hydrogen in the APT chamber, which is mostly protium ($^1$H). Additionally, using cryogenic sample transfer (cryo-transfer) in APT experiments helps preserve hydrogen signals after charging, ensuring sufficient data to identify trapping sites [21,30].

However, APT has limitations. Its field of view is typically not greater than 100 nm × 100 nm × 500 nm, although in some cases depths exceeding 1 μm have been achieved. That means it can typically observe only one type of hydrogen trap at a time, making it difficult to study and compare multiple types of traps under the same conditions [21,22]. Additionally, because APT experiments are destructive, it is impossible to observe the same microstructure before and after treatments like hydrogen desorption from heating, limiting our ability to research the trapping capability and dynamics of specific microstructures.

Given these challenges, this research aims to provide clear experimental evidence showing which microstructural features are the strongest hydrogen trapping sites in a strained pearlitic steel. Through a simple cold-drawing process, we developed a steel microstructure that incorporates both weak and strong hydrogen traps, as confirmed by TDS. We tested the hydrogen embrittlement susceptibility of the pearlitic steel samples and demonstrated reduced ductility loss (i.e., less embrittlement) in samples with strong traps after hydrogen charging, compared to those with only weak traps. To observe hydrogen trapping in APT, we developed a custom workflow that allowed us to produce APT specimens with highly consistent microstructures, including both the weak and strong traps, ensuring comparability across experiments. To distinguish weak and strong trapping sites, we conducted APT experiments with and without cryo-transfer, allowing us to observe hydrogen in both types of traps and only in strong traps, respectively. The results confirm that strong traps hold hydrogen for extended periods at room temperature. To further validate our APT findings, we performed numerical analyses based on our TDS results and the APT experiment parameters. Inconsistencies between the APT experimental data and conventional theories indicate that conventional hydrogen trapping models require revision. Our findings contribute to a deeper understanding of hydrogen trapping in metals and demonstrate a cost-effective, industry-ready process for creating strong hydrogen traps in steels, advancing the development of materials compatible with hydrogen use.

## 2. Experimental methods

### 2.1. Material

This research uses pearlitic steel wires with a composition of Fe–0.86C–0.72Mn–0.28Cr–0.24Si (weight percent) supplied by CITIC Metal. The wires underwent three different levels of strain via successive cold drawing. Compared to normal tensile approaches [31,32], successive cold drawn steels have fewer microcracks, which are known to be strong hydrogen traps and potential initiation sites for hydrogen embrittlement [3,33,34].

### 2.2. Electron microscopy characterizations

To characterize material microstructures, we employed scanning electron microscopy (SEM), electron backscatter diffraction (EBSD), scanning transmission electron microscopy (STEM), and transmission Kikuchi diffraction (TKD). SEM/EBSD specimens were mechanically grinded using silicon carbide (SiC) papers from 320 to 1200 grit before being further polished by the diamond suspensions with the particle sizes from 9, 3, to 1 μm. Then the specimens were polished using a Vibratory Polisher for 1 hour as the final step. TKD specimens were prepared by using twin-jet electropolishing in an Electropolisher TenuPol-5 with 10 volume percent of perchloric acid in ethanol at −20 °C and a voltage of 20 V. A Zeiss ULTRA Plus SEM with an Oxford Instruments Symmetry CMOS EBSD detector and an Aztec software was used to collect SEM/EBSD data, using an acceleration voltage of 20 kV and a step size of 50 nm. The TKD data was collected at an acceleration voltage of 30 kV with a step size of 5 nm.

STEM specimens were prepared by using xenon plasma focused ion beam (FIB) in a ThermoFisher G4 Hydra in the following order of ion-beam milling: 30 kV–300 pA, 30 kV–30 pA, and 5 kV–30 pA. A ThermoFisher Spectra S/TEM operated at 300 kV was used to obtain the STEM images with a convergence angle of 17.9 mrad and collection angles of 38 – 200 mrad for high-angle annular dark-field images (HAADF) and 9 – 35 mrad for annular bright-field (ABF) images.

### 2.3. Thermal desorption spectroscopy (TDS)

The TDS system at Shanghai Jiao Tong University was used in this

study, which contains a glass tube furnace, a vacuum pump, and a quadrupole mass spectrometer by INFICON with a home-made cryo-stage for minimizing hydrogen loss prior to measuring the desorbed hydrogen. Samples for TDS experiments were cut into 10 mm × 5 mm × 1 mm cuboids and then polished using SiC papers from 320 to 1200 grit. Subsequently, they were electrochemically charged with hydrogen using a 0.1 M NaOH + 1 g/L $NH_4SCN$ aqueous solution at a current density of 50 mA/cm$^2$ for 24 hours. After that, the hydrogen-charged specimens were placed on a cooling stage at approximately 5 °C in the loading chamber of the TDS instrument. Then the vacuum-pumping was started while the temperature of the cooling stage was continuously decreasing to approximately −190 °C before TDS experiments were conducted. This cooling and pumping process took approximately 20 minutes. When the loading chamber pressure reached $10^{-4}$ Pa, the TDS specimens were transferred onto a room-temperature stage in the analysis chamber constantly at approximately $10^{-7}$ Pa, ready for subsequent heating and simultaneous hydrogen measurement.

The hydrogen measurements were conducted after either 0 hour, 2 hours, or 12 hours of waiting/desorption in the analysis chamber at room temperature. The heating was conducted at either 100 °C, 150 °C, and 200 °C per hour and ended at 500 °C. The isothermal desorption experiment was conducted with no waiting at room temperature for 5.5 hours. The Kissinger model was used to estimate the hydrogen trapping/detrapping energy ($E_d$), using the following Eq. (1):

$$\frac{\partial \ln\left(\frac{\phi}{\left(T_p^{(i)}\right)^2}\right)}{\partial\left(\frac{1}{T_p^{(i)}}\right)} = -\frac{E_d^{(i)}}{R} \tag{1}$$

where $T_p^{(i)}$ is the $i^{\text{th}}$ peak temperature in TDS desorption profiles.

### 2.4. Slow strain rate tensile testing (SSRT)

SSRTs were conducted following the ASTM E8 standard for tensile tests of round bars and using an Instron 5567 and a strain rate of 5 × $10^{-5}$ per second. Most of the round bar SSRT specimens have gauge length and diameter of 10 mm and 2.5 mm, respectively, except the unstrained specimens that use a gauge length of 50 mm. The specimens were mechanically polished using SiC papers from 320 to 1200 grit. The mechanical testing results were normalized and compared using the Young's modulus of the unstrained specimens.

Three different treatments were applied on the SSRT specimens: uncharged, hydrogen-charged (H-charged), and hydrogen charged and then desorbed at approximately $10^{-5}$ Pa for 12 hours (12-hour desorption). At least 3 specimens were performed at each condition. For hydrogen charging, we used the method similar to that of the TDS experiments, i.e. using aqueous solution of 0.1 M NaOH + 1 g/L $NH_4SCN$ and a current density of 50 mA/cm$^2$ for 24 hours. The overall SSRT results are provided in Table S2.

### 2.5. Atom probe tomography (APT)

The APT tips were fabricated from 1 mm × 1 mm × 15 mm matchstick-shaped bars. All APT tips were fabricated using a dedicated workflow, as illustrated in Fig. 1, to ensure the incorporation of cementite lamella oriented in the APT analysis direction, which improves the success rate of APT analyses that incorporate heterogeneous layers. It also ensured the incorporation of the tangled dislocations near the surface of the cementite lamella. The initial rough electropolishing was performed in 25 volume percent perchloric acid in acetic acid at 10–20 V until the bars separated into two tips in the middle. As shown in Fig. 1A, fine electropolishing was then carried out under an optical microscope using 2 volume percent perchloric acid in butoxyethanol to create sharp tips. For the non-H-charged samples (Fig. S5A in the Supplementary Information), tip sharpening was conducted using a $Ga^+$ Zeiss Auriga FIB–SEM with three sequential ion-beam conditions: 30 kV–5 nA, 30 kV–1 nA, and then 30 kV–500 pA, before a final 5 kV–50 pA low-energy low-current for 25 seconds removed the ion-damaged layer. For all H-charged specimens, all tip preparations were performed using a xenon plasma-focused ion beam (PFIB) to minimize the galium influence as shown in [35].

APT data was acquired using a LEAP 4000 Si by CAMECA. All APT experiments were conducted with a voltage pulse frequency of 200 kHz, a pulse fraction of 20 %, a specimen temperature of 50 K, and a flight path length of 90 mm. APT reconstructions were processed with AP Suite software (Version 6.1) by CAMECA, using a detector efficiency of 57 % and an image compression factor of 1.65.

As shown in Fig. 1C, the specimen deuterium charging and cryo-transfer methods were adopted from our previous studies [23,25], with an addition cryo-FIB step in the cryo-transfer process. The APT specimens were prepared in advance by using FIB, and the deuterium charging was carried out in a cryo-transfer glove box (M.Braun Inertgas Systems). The charging solution consisted of 0.1 M NaOH in $D_2O$, and the deuterium charging was applied to the APT tips for 45 seconds at 2.2 V. This was followed by a plunge-freezing in liquid nitrogen and then the cryo-transfer process.

The cryo-prepared specimens were then transferred from the glove box to the PFIB using a cryogenic ultra-high vacuum (UHV) suitcase. The sharpening process was completed at a cryo-stage at a low temperature of approximately −190 °C. Three ion-beam conditions were used—30 kV–0.1 nA and 30 kV–30 pA—to remove ice and further refine and smooth the tip during the annular milling process. A final 5 kV–50 pA polishing was applied for 10 seconds to remove the possible ion-damaged layer. Finally, the APT specimens were transferred again using the UHV suitcase from the PFIB system to the APT system to begin the APT measurements.

For the APT experiments for the desorbed specimens, the charging time, solution, and voltage conditions were the same as those used for the cryo-APT procedures. After charging, the tips were immediately placed in the load lock at room temperature and kept there for 2 hours. The vacuum in the load lock reached approximately $10^{-3}$ Pa within 10 minutes and maintained a level of $10^{-4}$ Pa for about 0.5 hours, before

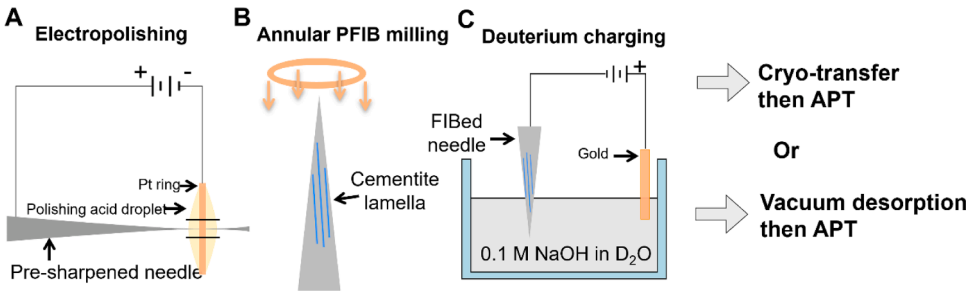


**Fig. 1.** APT tip specimen fabrication with vertical cementite lamella.

gradually decreasing to $10^{-5}$ Pa in the remainded time. The tips were then transferred to the analysis chamber via the buffer chamber before APT measurement commenced.

### 2.6. Calculation

The numerical models in this research mainly adapted the framework developed in [11,14,15,36–39]. The Kissinger approach for estimating the hydrogen trapping energy is shown in Eq. (1). Note that in Eq. (1) only the heating rate $\phi$ and the temperature are considered for the estimation of hydrogen binding energies. That is, the Kissinger model does not consider the effects of thickness, trapping densities, and initial hydrogen concentration, which are thus questionable in the estimation of binding energy. On the other hand, Oriani's and McNabb-Foster's models resolve the hydrogen diffusion process as well as the trapping kinetics.

For developing McNabb-Foster-Oriani model, we first consider the transport of hydrogen atoms inside the metal follows the Fick's second law:

$$\frac{\partial C}{\partial t}+\nabla\cdot\boldsymbol{J}=0 \tag{2}$$

where $C$ is the total hydrogen concentration and $\boldsymbol{J}$ is the flux. The total hydrogen concentration can be separated into the local concentration in the lattice ($C_L$) and in the trapping sites ($C_T$). Thus, Eq. (2) can be re-written as:

$$\frac{\partial C_L}{\partial t}+\frac{\partial C_T}{\partial t}+\nabla\cdot\boldsymbol{J}=0 \tag{3}$$

The flux $\boldsymbol{J}$ is defined as:

$$\boldsymbol{J}=-D_L\nabla C_L \tag{4}$$

where $D_L$ is temperature-dependent ideal diffusivity through lattice sites.

When multiple trapping sites are considered, the rate term can be defined as:

$$\frac{\partial C_T}{\partial t}=\sum_{i=1}^{n}\frac{\partial C_T^i}{\partial t} \tag{5}$$

Combining Eqs. (2)–(5), one can reach:

$$\frac{\partial C_L}{\partial t}+\sum_{i=1}^{n}\frac{\partial C_T^i}{\partial t}+\nabla\cdot(-D_L\nabla C_L)=0 \tag{6}$$

Consider now the definition of $\partial C_T/\partial t$, the general equilibrium equation for the $i^{th}$ trap site is given by the *McNabb-Foster* equation:

$$\frac{\partial C_T^{(i)}}{\partial t}=\left[k^{(i)}\theta_L N_T^{(i)}\left(1-\theta_T^{(i)}\right)-p^{(i)}C_T^{(i)}\left(1-\theta_L\right)\right] \tag{7}$$

with

$$k^{(i)}=\nu_t^{(i)}\exp\left(-\frac{E_t^{(i)}}{RT}\right)\ \text{and}\ p^{(i)}=\nu_d^{(i)}\exp\left(-\frac{E_d^{(i)}}{RT}\right) \tag{8}$$

where $T$ is the temperature, $R$ the gas constant, $\theta_L=C_L/N_L$ and $\theta_T=C_T/N_T$ are the occupancy fractions of hydrogen in the lattice and trapping sites, with $N_L$ and $N_T$ being the number of interstitial sites per unit volume and the trapping density, respectively. $E_d$ is the activation energy for moving from a lattice site to a trap site, while $E_t$ is the activation energy required for moving from a trap site to a lattice site. $\nu_d$ and $\nu_t$ are the vibration frequency of the hydrogen atom hopping from a lattice site to a trap and from a trap to a lattice site, respectively.

A commonly used assumption for describing trapping behaviors is that trap kinetics occur on a much smaller time scale than the diffusion of hydrogen through the lattice. Consequently, the time derivative in Eq. (7) is considered to be zero. By assuming $\nu_d^{(i)}=\nu_t^{(i)}=\nu$, one can reach the so-called *Oriani's local equilibrium* theory:

$$\frac{\theta_T^{(i)}}{1-\theta_T^{(i)}}=\frac{\theta_L}{1-\theta_L}K_T^{(i)} \tag{9}$$

and the equilibrium constant $K_T^{(i)}$, is given by:

$$K_T^{(i)}=\exp\left(\frac{-\Delta H^{(i)}}{RT}\right) \tag{10}$$

with $\Delta H^{(i)}=E_t^{(i)}-E_d^{(i)}$ being the trap binding energy.

Following Eq. (9) and considering the very low solubility of hydrogen in the lattice ($\theta_L\ll1$), the concentration of trapped hydrogen can be expressed as:

$$C_T^{(i)}=\frac{K_T^{(i)}N_T^{(i)}\theta_L}{1+K_T^{(i)}\theta_L} \tag{11}$$

Subsequently, the rate term can be expressed as:

$$\frac{\partial C_T^{(i)}}{\partial t}=\frac{\partial C_T^{(i)}}{\partial C_L}\frac{\partial C_L}{\partial t}+\frac{\partial C_T^{(i)}}{\partial K_T^{(i)}}\frac{\partial K_T^{(i)}}{\partial T}\frac{\partial T}{\partial t} \tag{12}$$

Note that the second term in Eq. (12) is only applicable to the TDS test (Fig. 7A). For experiments that involve a constant room temperature (Fig. 7B-E), this term is zero and can be naturally omitted. In the TDS experiments, the temperature increases from $T_0$ at a constant heating rate $\phi$; thus, Eq. (12) can be formulated as,

$$\frac{\partial C_T^{(i)}}{\partial t}=\frac{K_T^{(i)}N_T^{(i)}/N_L}{\left(1+K_T^{(i)}C_L/N_L\right)^2}\frac{\partial C_L}{\partial t}+\frac{N_T^{(i)}K_T^{(i)}\Delta H^{(i)}\phi\left[C_L/N_L-\left(C_L/N_L\right)^2\right]}{RT^2\left[1+K_T^{(i)}C_L/N_L\right]^2} \tag{13}$$

Also, a non-dimensional operational diffusivity $D^*$ can be defined as:

$$D^*=1+\sum_{i=1}^{n}\frac{K_T^{(i)}N_T^{(i)}/N_L}{\left(1+K_T^{(i)}C_L/N_L\right)^2} \tag{14}$$

Considering the simulation of the TDS test is a one-dimensional problem in the case of sheet specimens, i.e., the thickness $L$ of the specimen is much smaller than the other two dimensions, the *Oriani's local equilibrium* can be re-written by combining Eqs. (6), (13), and (14), leading to:

$$D^*\frac{\partial C_L}{\partial t}+\sum_{i=1}^{n}\frac{N_T^{(i)}K_T^{(i)}\Delta H^{(i)}\phi\left[C_L/N_L-\left(C_L/N_L\right)^2\right]}{RT^2\left[1+K_T^{(i)}C_L/N_L\right]^2}=\frac{\partial}{\partial x}\cdot\left(D_L\frac{\partial C_L}{\partial x}\right) \tag{15}$$

which is the governing equation for the TDS simulation in Fig. 7A. Note that Eq. (15) is equivalent to Eqs. (6)–(8) when the values of the vibration frequencies $\nu_d^{(i)}$ and $\nu_t^{(i)}$ are set to sufficiently large values; these vibration frequencies are expected to be on the order of the Debye frequency ($10^{13}$ Hz). Also, the diffusion coefficient, $D_L$, is a temperature-dependent function, which defines as:

$$D_L=D_0\exp\left(\frac{-E_t}{RT}\right) \tag{16}$$

For Fig. 7B-D with a constant temperature, the governing equation becomes,

$$\left[1+\sum_{i=1}^{n}\frac{K_T^{(i)}N_T^{(i)}/N_L}{\left(1+K_T^{(i)}C_L/N_L\right)^2}\right]\cdot\frac{\partial C_L}{\partial t}=D_L\nabla^2C_L \tag{17}$$

And the parameters in Table S3 and specimen dimensions in Fig. S9 were used in our simulation. Based on the parameters defined above, we compare the TDS curve predictions in Fig. 7A using the Oriani model and the McNabb-Foster model. For the McNabb-Foster model, the vibration frequencies $\nu_d^{(i)}$ and $\nu_t^{(i)}$ are set to be the Debye frequency, $\nu_d^{(i)}=$

$\nu_t^{(i)} = 10^{13}$ Hz, as it is commonly assumed [65]. As shown in Fig. S10, both models yield identical results, demonstrating the consistency between these two theories. This is consistent with literature results, which show that Oriani's equilibrium generally holds [65].

## 3. Results and discussion

### 3.1. Material microstructure

As shown schematically in Fig. 2A, three pearlitic steel wires were used, denoted as unstrained (black), mid-strained (blue), or high-strained (red) with diameters of 13 mm, 8 mm, and 5.6 mm, respectively. The microstructural evolution with successive cold drawing was characterized using SEM, EBSD, STEM, and TKD. Fig. 2B-D are EBSD inverse pole figure maps for the unstrained, mid-strained, and high-strained specimens, respectively. Here, RD, ND, and TD represent the rolling/drawing direction, the normal direction (perpendicular to the displayed plane), and the transverse direction. These figures show a grain size reduction from 27.6 μm, to 6.77 μm, and further to 2.19 μm as cold drawing progresses, indicating a higher density of grain boundaries. Fig. 2E-G display geometrically necessary dislocations (GNDs) maps for the three specimens, revealing that as strain increases, the crystallographic misorientation and thus the density of geometrically necessary dislocations increases from 9.78, to 18.41, and 25.49 (units: $10^{14}$ $m^{-2}$). Additional EBSD pole figures of all three specimens are provided in the Supplementary Information (Fig. S1).

Fig. 2H-J show STEM annular bright-field images of the unstrained, mid-strained, and high-strained specimens. These images contain cementite lamella (yellow arrows), dislocations (magenta arrows), and the ferrite matrix (green arrows). The dislocation density appears to increase at greater strain levels, which aligns with the GNDs results (Fig. 2E-G). In Fig. 2I and J, tangled dislocations can be seen at the proximity of the cementite-ferrite interfaces, and in the high-strained specimen, some of the cementite lamellae appear sheared, Fig. 2J.

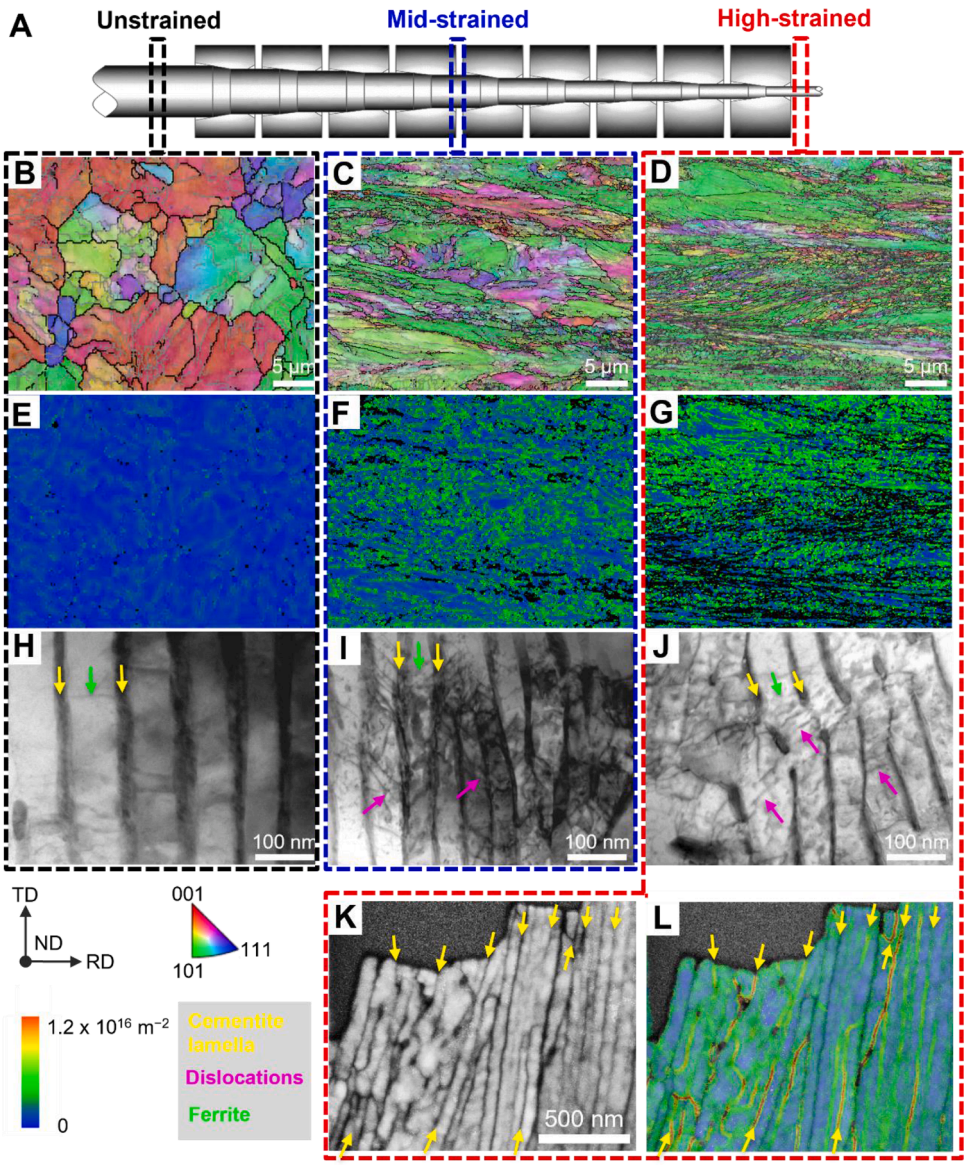


**Fig. 2.** Strain-induced microstructural changes in pearlitic steel samples. (A) illustrates the cold drawing process used for straining the pearlitic steel wire samples and the unstrained (black, 13 mm diameter), mid-strained (blue, 8 mm diameter), and high-strained (red, 5.6 mm diameter) states. (B–D) are EBSD inverse pole figures, overlaying band contrast and grain boundary maps, from the three samples. (E–G) are geometrically necessary dislocations (GNDs) maps showing dislocation density. (H–J) are STEM ABF images of the three specimens along the [110] zone axis. (K–L) are TKD results from a high-strained specimen. (K) is a band contrast map overlaid with a grain boundary map. (L) is the GNDs dislocation density map.

Further analysis of the dislocation structures at the cementite-ferrite interface was conducted using high-resolution STEM as provided in the Supplementary Information (Fig. S2), which confirms the presence of dislocations at these interfaces. These findings are consistent with the literature that have reported similar microstructural evolution resulting from straining pearlitic steels [31,32,34,40–42].

To provide a more comprehensive view of the dislocation distribution near the cementite-ferrite interfaces, we performed TKD analysis on a single pearlite grain from the high-strained specimen, as shown in Fig. 2K and L Fig. 2K is a band contrast image showing the location of the cementite lamella (yellow arrows). Fig. 2L presents the corresponding GNDs map, which shows a correlation between the cementite lamella and regions of high dislocation density in ferrite, further confirming the presence of dislocations near the cementite-ferrite interfaces in the strained specimens. The findings lay the groundwork for further analyses of hydrogen trapping behavior, and how this relates to the microstructural changes upon straining in the pearlitic steel specimens.

### 3.2. Strong and weak hydrogen traps

As shown in Fig. 3, we used TDS to compare hydrogen trapping in the unstrained (Fig. 2H) and high-strained specimens (Fig. 2J and L), where the main microstructural differences are the grain size and the presence of tangled dislocations. After electrolytically saturating the TDS specimens with hydrogen, we conducted hydrogen desorption in a high vacuum chamber at $10^{-7}$ Pa at room temperature, for three different durations: 0 hour (i.e., no desorption), 2 hours or 12 hours. The goal was to test the effectiveness of the tangled dislocations as strong hydrogen traps at room temperature. All the measured contents of hydrogen are provided in Table S1 in the Supplementary Information.

Fig. 3A shows the hydrogen desorption profiles for the unstrained specimens after no desorption (black), 2-hour desorption (blue), and 12-hour desorption (red). The data from the unstrained specimens contain a single hydrogen desorption peak at approximately 100 °C, which decreases as the sample desorption time increases. Fig. 2B shows the hydrogen desorption profiles for the high-strained specimens after different desorption periods. These profiles contain *two* hydrogen desorption peaks—one at approximately 100 °C (low-temperature peak) and the other at 240 °C (high-temperature peak).

Note that Fig. 3A uses a different y-axis scale compared to Fig. 3B, and the low-temperature peak is associated with much more hydrogen for the strained sample than the unstrained sample. This low temperature peak is consistent with the type of peak usually created from trapping of hydrogen at weak traps, including grain boundaries [18,33,43], and is consistent with the change of grain boundary density revealed by Fig. 2B and D Complete hydrogen contents measured by TDS can be found in Table S1 in the Supplementary Information.

Fig. 3C is a close-up image of the high-temperature desorption peak, showing that it does not decrease significantly with longer desorption times (blue and red profiles). This suggests that the stronger hydrogen traps observed in the strained samples are highly effective in retaining hydrogen over extended periods. Data for the mid-strained specimens, as shown in Fig. S3 in Supplementary Information, agrees well with the results for the high-strained specimens that have a similar microstructure (Fig. 2B). Overall, our TDS results are in good agreement with the results reported in the literature that also used TDS for studying hydrogen trapping in pearlitic steels [17,33,40].

We used the TDS data to estimate the hydrogen detrapping energies for these pearlitic steel samples, which can serve as an approximation of the trapping binding energies in the body-centered cubic (BCC) steels like the one used in this research, due to the low lattice diffusion barrier for the hydrogen in these materials [3]. As shown in Fig. 3D, we used three heating rates—100 °C per hour, 150 °C per hour, and 200 °C per hour—to generate the corresponding desorption profiles. From these, we estimated the detrapping energies to be 30.2 kJ/mol and 47.0 kJ/mol for the low- and high-temperature peaks, respectively, Fig. 3E, based on the conventional one-step hydrogen detrapping model [18,20]. It is important to note that the low-temperature peak may include contributions from other weak traps, such as dislocations [18,43], vacancies [44,45], and other microstructures [3,9]. However, this study

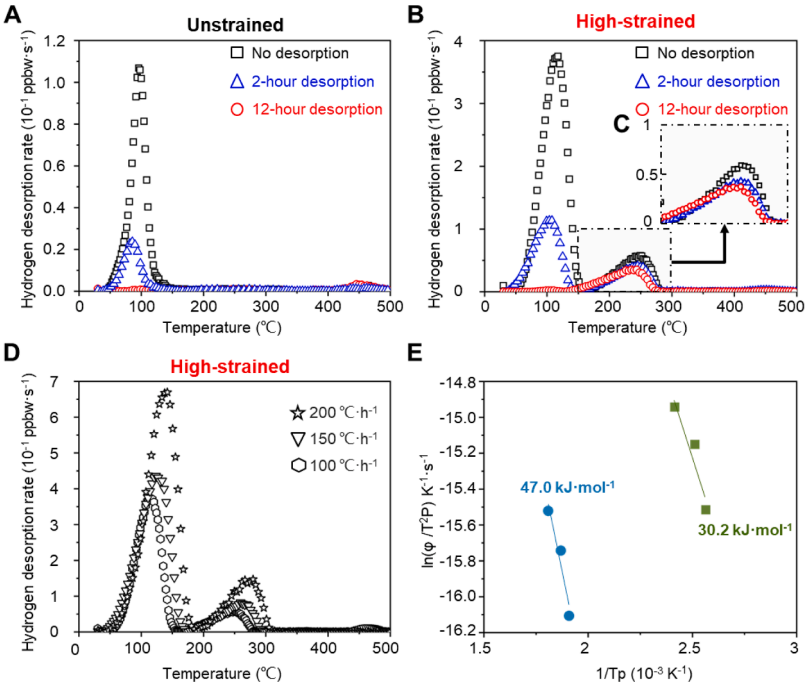


**Fig. 3.** Hydrogen trapping in unstrained and high-strained specimens. Hydrogen TDS profiles of results of (A) unstrained and (B) high-strained specimens that are either undergoing no desorption (black), 2 hours of desorption (blue), or 12 hours of desorption (red) at room temperature. (C) Magnified view of the black dashed area in Figure (B). (D) Hydrogen TDS profiles of high-strained specimens under three different heating rates: 100 °C per hour (hexagon), 150 °C per hour (triangle) and 200 °C per hour (star). (E) Kissinger plots to estimate hydrogen detrapping energies corresponding to the high-temperature (blue) and low-temperature (green) hydrogen desorption peaks in Figure (D).

focuses on identifying the source of the strong hydrogen traps responsible for the high-temperature peak. As such, no further attempts were made to deconvolute the individual contributions of these weak traps, given that this remains a challenging task [3,9].

### 3.3. Hydrogen embrittlement susceptibility

With an understanding of material microstructures and macroscopic hydrogen trapping, we evaluated the hydrogen embrittlement susceptibilities of the pearlitic steel specimens using SSRT. Two different treatments were applied to the SSRT specimens for comparison with the uncharged reference: hydrogen-charged and then immediately tested (H-charged), and hydrogen charged followed by 12 hours of desorption in vacuum (12-hour desorption). The representative stress-strain curves for the uncharged reference, H-charged state, and 12-hour desorption states are shown in Fig. 4, in black, blue, and red, respectively. The vertical and horizontal bars in Fig. 4 indicate the ranges of ultimate tensile strength and total elongation, respectively, from three measurements for each sample condition.

In Fig. 4, the uncharged data (black) shows the high-strained pearlite steel specimens have significantly higher ultimate tensile strengths (UTS), reaching approximately 2.2 gigapascals (GPa), compared to the unstrained specimens, which have UTS of around 1.3 GPa. This increase in UTS results from a combination of grain refinement (Fig. 2B-D) and increased dislocation density (Fig. 2E-G), and a higher carbon content in the BCC steel matrix, which is well documented in literature [31,40,42,46,47]. Complete mechanical property data can be found in Table S2 in the Supplementary Information.

To quantify hydrogen embrittlement susceptibility, we measured the ductility loss, defined as the reduction in elongation compared to the uncharged state:

$$Ductility\ loss\ (\%) = \frac{Elongation_{\ uncharged} - Elongation_{\ H-charged}}{Elongation_{\ uncharged}}$$

Based on this metric, we found the average ductility loss for the high-strained specimens was 14.4 % (magenta arrow, top curves in Fig. 4), which is lower than the 22.1 % ductility loess observed in the unstrained specimens (green arrow, bottom curves in Fig. 4). This result is noteworthy because the reduction in ductility loss in the stronger material contradicts the conventional understanding of hydrogen embrittlement susceptibility, which generally suggests the high-strength materials are more susceptible [2,3,9,48]. In fact, steels with similarly high strength (approximately 2 GPa) have often been reported to suffer from 50 to 90 percent of ductility loss in the presence of hydrogen [8,49–51]. Our finding that the strained pearlitic steel exhibits low embrittlement susceptibility aligns with studies of similar materials in literature [31,33,40,52].

In addition to the H-charged specimens, we also tested the 12-hour desorption specimens, as shown by the red broken lines in Fig. 4. These specimens demonstrated a recovery in ductility after weakly trapped hydrogen was removed. We further conducted fracture surface observation using SEM, as shown in Fig. S4 in the Supplementary Information. The SEM results revealed more brittle cleavage in the H-charged specimens than in the uncharged and desorbed specimens, consistent with the mechanical results shown in Fig. 4 and the results reported in literature with strained pearlitic steel samples [17,31,33,40,52].

In summary, we found the high-strained pearlitic steel sample can accommodate more hydrogen (Fig. 3), while showing a higher resistance to hydrogen embrittlement (less ductility loss) and simultaneously exhibiting greater strength, compared to its unstrained counterpart (Fig. 4). This is attributed to the presence of strong hydrogen traps (Fig. 3B), which reduce hydrogen's involvement in crack initiation and propagation. To further explore this, we used APT to investigate how hydrogen interacts with the microstructure of the high-strained pearlitic steel, aiming to identify which microstructures contribute to its low embrittlement susceptibility.

### 3.4. Observation of weak and strong hydrogen traps

To observe and differentiate between weak and strong hydrogen traps in the high-strained pearlitic steel, we conducted two types of APT experiments. One used cryo-transfer, which preserves both weakly and strongly trapped hydrogen for observation. Another one included a vacuum desorption process at room temperature without using cryo-transfer, leaving only strongly trapped hydrogen for observation.

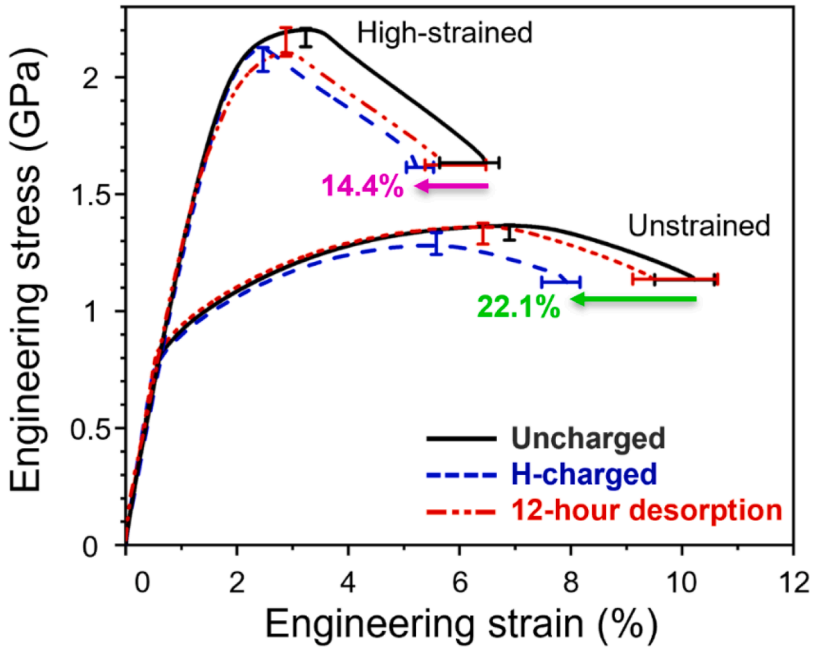


**Fig. 4.** SSRT stress-strain curves of high-strained and unstrained specimens for hydrogen embrittlement susceptibility. Black, blue, and red refer to uncharged, hydrogen-charged and tested immediately (H-charged), and hydrogen-charged desorbed for 12 hours at room temperature in vacuum (12-hour desorption). The error bars refer to ultimate tensile strength and elongation, which are obtained from 3 data points for each condition.

After tip fabrication, the APT specimens were electrolytically saturated with deuterium before undergoing either cryo-transfer, initiated by a plunge-freezing in liquid nitrogen, or room-temperature desorption in the APT vacuum chamber for 2 hours. During the desorption process, the progress of hydrogen desorption was monitored in real time using the vacuum chamber's pressure gauge. The hydrogen-charged, non-cryo specimens consistently required approximately 10 minutes longer at $10^{-3}$ Pa to reach the normal operating pressure of $10^{-5}$ Pa compared to uncharged reference specimens. The APT mass spectra of uncharged, cryo-transfer, and hydrogen-desorbed specimens are respectively provided in Fig. S5A-C in the Supplementary Information, which also shows the ion labeling method in APT data analyses.

Fig. 5 shows the APT results of a deuterium-charged, cryo-transfer specimen. Fig. 5A is an overall image of a reconstructed 3-dimensional atom map, showing the distribution of carbon (C, blue) and deuterium (D, red) atoms, where the carbon-rich regions are cementite lamella. Fig. 5B is a slice view from the y-z plane marked in Fig. 5A, which shows a clear correlation between the distribution of the deuterium and carbon atoms, suggesting hydrogen trapping in (and near) cementite lamella. Fig. 5B also shows a ridge in the carbon distribution, indicated by the orange arrow, thought to be a sheared cementite lamellar, as seen in the previous TEM image (Fig. 2J). Fig. 5C is an elemental concentration profile from a cylindrical region of interest (ROI) marked by the black dashed lines in Fig. 5B, showing an increased carbon content and decreased of iron (Fe, grey) content, across a cementite plate. These changes also coincide with an increase of deuterium content, indicating hydrogen trapping. This observation of hydrogen trapping in cementite lamella is consistent with our previous research studying an unstrained pearlitic steel specimen [53].

Fig. 5D-F are cross-sectional views from the respective x-y planes marked in Fig. 5A, using 2 atomic percent (at. %) carbon iso-concentration surfaces (isosurfaces) [23,54] to delineate the cementite regions. These delineations offer a clearer view of the shapes of the cementite lamella and their surroundings. We found carbon-rich regions that connect the cementite lamella, highlighted by magenta arrows in Figs. 5D and 4E. These regions are thought to be the footprints of dislocation shearing across the cementite lamella, which is well-documented in literature [34,41,55]. Fig. 5F shows that these dislocation-sheared carbon-rich regions are only present in specific areas and are not uniform along the cementite lamella, ruling out artifacts in APT.

Hydrogen trapping in the cementite lamella (Fig. 5) is attributed to a combination of carbon vacancies [34,56], interstitial hydrogen in solution, and the presence of tangled dislocations near the cementite-ferrite interfaces (Fig. 2G and J) [31]. A couple of notes when interpreting these images. First, dislocations without elemental segregation are not visible in APT data. In the case that dislocations attract carbon in the form of "Cotrell atmospheres" [41,55,57–59], dislocations can also attract hydrogen has been demonstrated in literature [23,24]. Second, trajectory aberrations at interfaces in atom probe data can lead to "blurring" of compositions across interfaces and this effect is strongest if the boundaries are oriented in the analysis direction [55,60], as they are in these experiments. This means that the carbon isosurfaces in Fig. 5D-F are a guide to carbon-rich areas, but do not indicate the exact locations of the cementite-ferrite interfaces. The relatively low carbon concentration (5.7 at. %) observed within the cementite lath of the strained sample shown in Fig. 5C is attributed to deformation-induced cementite decomposition [41,61] . An additional uncharged APT dataset in Fig. S6 shows that the degree of decomposition may vary across different cementite laths and different locations within one lath, indicating an inhomogeneous decomposition potentially caused by localized strain [41,47,61].

Fig. 6 shows the atom maps from the desorbed deuterium-charged specimen, which are quite different to the cryo-transfer specimen results in Fig. 5. Fig. 6A is an overall 3-dimensional atom map of the carbon and deuterium. Fig. 6B is a slice view from the y-z plane marked in Fig. 6A, and C is a concentration profile for the ROI marked in Fig. 6B D-6F show slices from the respective x-y planes marked in Fig. 6A. These indicate a concentration of hydrogen near the cementite-ferrite interface, contrasting with the co-localization of hydrogen and carbon observed in the cryo-transfer APT specimen. A repeat APT experiment on the 2-hour hydrogen-desorbed specimen is shown in Fig. S7 in the Supplementary Information, which agrees well with the results in Fig. 6. Additionally, we conducted a 1-hour desorption experiment (Fig. S8 in

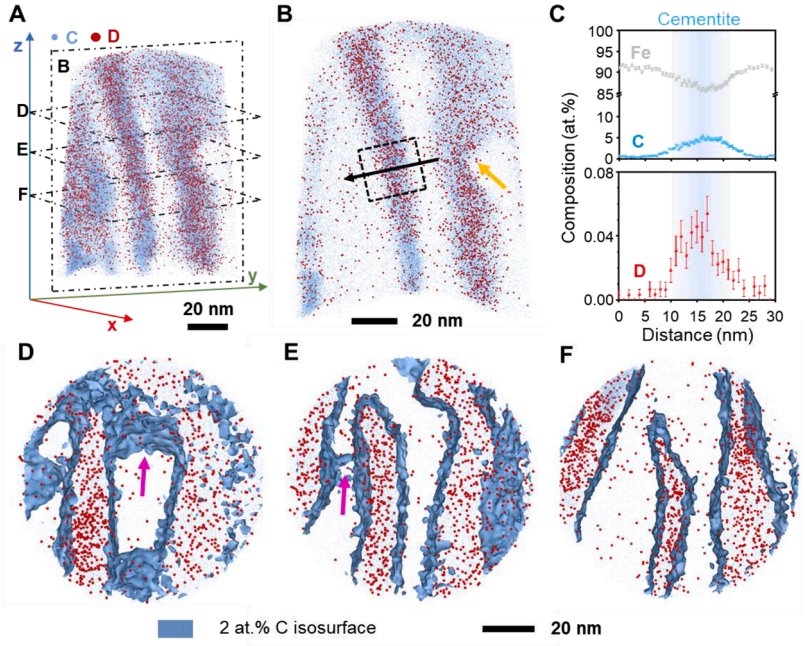


**Fig. 5.** Hydrogen maps of cryo-transfer strained steel specimen. (A) is a reconstructed 3-dimensional atom map, where carbon (C) and deuterium (D) atoms are shown in blue and in red, respectively. (**B**) is a 10-nm-thick slice view of the region in the y-z plane marked by the black dashed lines in (A). (**C**) provides the elemental concentrations of iron (grey), carbon (blue), and deuterium (red) from the 30 nm x 30 nm cylindrical ROI marked by the black dashed lines in (B). (**D–F**) are 10-nm-thick slices from the x-y planes marked by the dashed lines in (A), using 2 atomic percent carbon isosurfaces to highlight the carbon-rich regions.

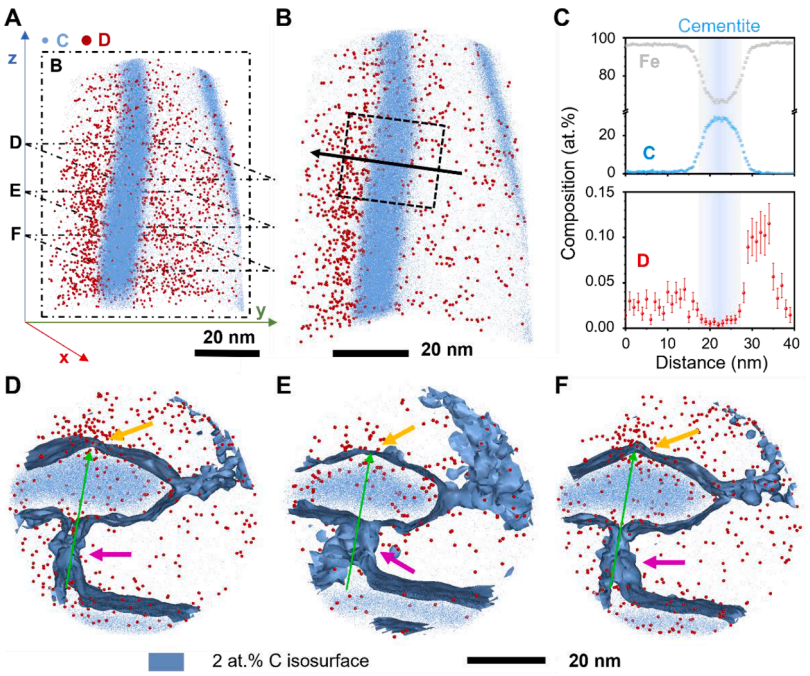


**Fig. 6.** Hydrogen maps of hydrogen-desorbed strained steel specimen. (A) is a reconstructed 3-dimensional atom map, where carbon (C) and deuterium (D) atoms are shown in blue and in red, respectively. (**B**) is a 10-nm-thick slice view of the region in the y-z plane marked by the black dashed lines in (A). (**C**) provides the elemental concentrations of iron (grey), carbon (blue), and deuterium (red) from the 30 nm x 40 nm cylindrical ROI marked by the black dashed lines in (B). (**D–F**) are 5-nm-thick slices from the x-y planes marked by the dashed lines in (A), using 2 atomic percent carbon isosurfaces to highlight the carbon-rich regions.

the Supplementary Information), which yielded similar hydrogen distribution patterns, suggesting the observed hydrogen distributions in these specimens are stable. These findings are consistent with literature that used either APT [32,62] or another technique (silver microprint) [31,52] and showed similar hydrogen localization near cementite-ferrite interfaces.

The APT results in Figs. 5 and 6 suggest that the room-temperature desorption allowed the release of hydrogen trapped in the cementite lamella, but not the hydrogen that is trapped close to the cementite-ferrite interface. This indicates that cementite has a lower hydrogen trapping ability than the features near the cementite-ferrite interfaces. Of course, hydrogen retention depends on specimen size [28,63]. It is notable that such small APT specimens can retain significant hydrogen at room temperature for such a long duration (2 h). Based on the microstructure of the high-strained specimens (Fig. 2I, J, and L), we conclude that the strong hydrogen trapping observed at the interface is associated with tangled dislocations near the cementite-ferrite interfaces. This is supported by the APT slice views (Fig. 6D-F), which show interesting hydrogen clusters near a cementite ridge (orange arrows) that align with the direction of dislocation-shearing footprints (green arrows) identifiable by the carbon between the cementite lamella (magenta arrows).

In summary, comparing hydrogen-preserved (cryo-transfer) and hydrogen-desorbed APT results (Figs. 5 and 6), we confirm the presence of strong hydrogen traps near the cementite-ferrite interfaces in highly strained pearlitic steel specimens, where abundant tangled dislocations are present, as indicated by TKD (Fig. 2L) and STEM (Fig. 2I and J). Considering the high density of tangled dislocations, we believe these traps are the primary contributors to the high-temperature hydrogen desorption peak observed in the TDS data (Fig. 3B). Notably, these tangled dislocation traps can be produced in large quantities through straining at low cost, offering significant advantages over other traps like carbide precipitates, which require alloying elements [49,64]. Moreover, we found that the hydrogen trapped in cementite lamella was released after room-temperature desorption, indicating that cementite is a weaker trap compared to tangled dislocations. This type of weak hydrogen trapping, observed using APT, has rarely been reported due to the extreme sensitivity of small APT specimens to heat during sample transfer, requiring careful cryo-workflow design and execution [21,30]. By combining cryo-transfer and room-temperature desorption experiments on the highly strained pearlitic steel specimens, we reconcile discrepancies in the literature regarding hydrogen trapping sites in steels [32,53,62].

### 3.5. *Correlating TDS and APT with conventional desorption models*

Numerical analyses were carried out to correlate our APT and TDS results with conventional hydrogen trapping/detrapping theories, with an aim to quantify the effective trapping and detrapping energies of the tangled dislocation strong traps. Three foundational theories are considered here: the Kissinger single-step hydrogen detrapping model [20] and the more rich Oriani and McNabb-Foster hydrogen trapping and diffusion models [15,65]. Note that we compared both predictions from Oriani and McNabb-Foster theories, finding that both models retrieve the same result (Fig. S10). Therefore, only one set is shown in the main text.

Our first goal was to simulate a TDS desorption profile consistent with the high-strained specimen TDS data shown in Fig. 3B, by using the Oriani/McNabb-Foster hydrogen models with input parameters from either the literature or our experiments, as provided in Table S3 in the Supplementary Information. Specifically, we used the low and high detrapping activation energies extracted from our TDS data (Fig. 3D)—30.2 kJ/mol and 47 kJ/mol, respectively—obtained through the Kissinger single-step detrapping model. However, the simulation result failed to match the TDS experimental data, particularly for the high-temperature peak associated with the 47 kJ/mol detrapping energy. This was expected as the Kissinger model has been empirically known to underestimate trap binding energies [66]. To address this discrepancy, we refined our simulation by introducing a higher detrapping activation energy of 80 kJ/mol for the high-temperature peak, a value selected based on studies in the literature that examined similar materials [17,33]. This adjustment resulted in the solid line shown in Fig. 7A, which

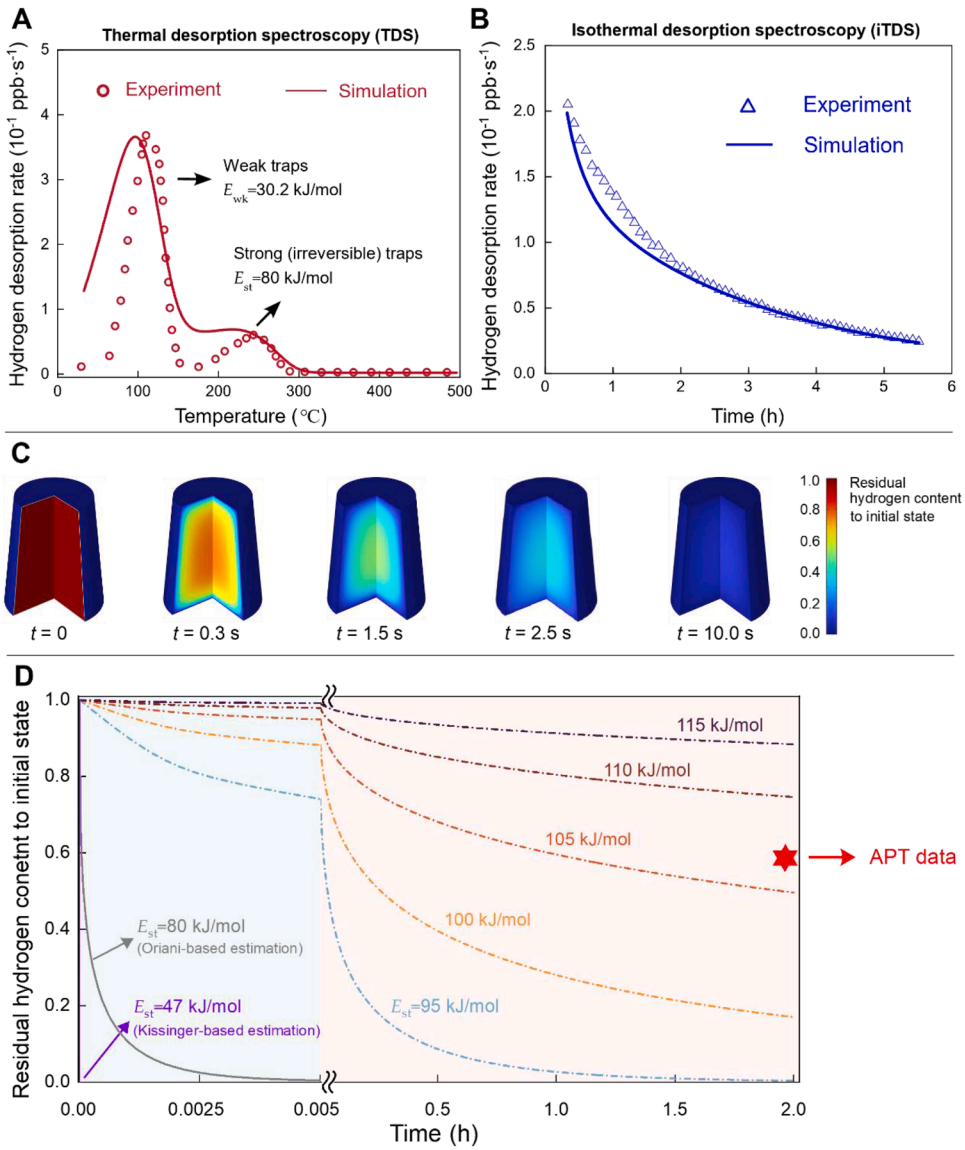


**Fig. 7.** Numerical simulations of hydrogen desorption using the Oriani/McNabb-Foster model. (A) shows the simulated (solid line) and experimental (spheres) TDS results considering the presence of two hydrogen traps of 30.2 kJ/mol and 80 kJ/mol. (**B**) shows the simulated (solid line) and experimental (triangles) isothermal desorption spectroscopy (iTDS) results considering the presence of two hydrogen traps of 30.2 kJ/mol and 80 kJ/mol. (**C**) shows a simulated process of hydrogen desorption from a APT specimen. (**D**) shows the simulated desorption profiles in the presence of a variety of strong hydrogen traps, from 47 to 115 kJ/mol, as well as the APT residual hydrogen content based on the cryo-transfer APT data and the 2-hour desorption data. Note that the purple line is located close to the Y-axis.

aligns with the TDS data, represented by the spheres.

Using an 80 kJ/mol detrapping energy for the high-temperature desorption peak along with the Oriani/McNabb-Foster hydrogen diffusion model, we generated a hydrogen isothermal desorption spectroscopy (iTDS) profile considering the dimension of TDS specimens, shown as the solid line in Fig. 7B Unlike conventional TDS, which continuously increases temperature, this approach better reflects the conditions of our APT desorption experiments at ambient temperature. We compared this model with high-strained specimen data (triangles in Fig. 7B), measured at room temperature over 5.5 hours. We found using 30.2 and 80 kJ/mol yielded a strong correlation, affirming our simulation's accuracy for TDS bulk specimens.

Next, we considered the dimension of the APT specimens (see Fig. S9 in the Supplementary Information) and the presence of both 30.2 kJ/mol and 80 kJ/mol hydrogen traps in our model. As shown in Fig. 7C, the model predicted that hydrogen desorbs within 10 s in this configuration, contradicting the APT results where hydrogen remained trapped by tangled dislocations after 2 hours. To resolve this inconsistency, we explored a range of detrapping energies for hydrogen desorption in an APT specimen, varying from 47 kJ/mol to 115 kJ/mol, as shown in Fig. 7D, using the Oriani/McNabb-Foster model.

Fig. 7D is displayed with two different x-axis scales to better view the desorption times for lower detrapping energies (i.e., 47 kJ/mol and 80 kJ/mol). The purple (47 kJ/mol) and grey (80 kJ/mol) lines suggest that full hydrogen desorption in a volume at APT specimen size would occur within 0.0005 and 10 seconds, respectively, which does not align with the APT results. This suggests that neither 47 kJ/mol nor 80 kJ/mol accurately describes the trapping and detrapping behaviors of the tangled dislocations.

We then compared the global hydrogen content in both the cryo-transfer APT specimen (Fig. 5) and the 2-hour desorbed specimen (Fig. 6). The ratio of these hydrogen contents, representing the residual hydrogen after 2 hours of desorption, is shown by the red star in Fig. 7D This data point falls between the simulated results for detrapping energies of 105 and 110 kJ/mol, suggesting that the tangled dislocations may have an effective detrapping energy exceeding 105 kJ/mol, which

is considerably high compared to reported values in the literature [3,9,67]. We suspect that this high effective detrapping energy results from a combination of the intrinsic trapping energy of dislocations and the re-trapping of detrapped hydrogen, a concept that has been hypothesized [68] but currently lacking direct experimental support. Regardless, our results showcase the potential of using APT in future research to prove this hypothesis. More importantly, our APT results indicate the tangled dislocation traps appear to have much higher potency, i.e., sequester hydrogen for much longer, than existing theories predict.

## 4. Conclusion

Our work makes the following contributions. First, we clarify the distinct roles of strong and weak hydrogen traps, identifying tangled dislocations as effective, stable hydrogen traps that mitigate embrittlement susceptibility in steels. Second, we provide the first experimental observations of strong hydrogen trapping by employing APT with cryo-transfer and controlled desorption, adding critical empirical evidence to the theoretical landscape of hydrogen trapping. Third, our findings challenge the conventional understanding around local equilibrium theory [14,15], which assumes hydrogen release from traps aligns with surrounding concentration levels, may not fully apply in engineering materials with complex nanostructures. We demonstrate that tangled dislocations retain hydrogen effectively over extended periods, challenging the conventional belief in the ineffectiveness of hydrogen trapping for embrittlement mitigation. Lastly, we showcase the use of cryo-APT combined with controlled desorption offers a new, comprehensive methodology to map hydrogen trapping in metal matrices, ensuring accurate differentiation between hydrogen traps. This method represents an essential tool for future studies aiming to understand hydrogen behaviors in materials. In summary, our research provides new perspectives on the design of hydrogen-resistant steels and underscores the potential of defect engineering as a cost-effective and sustainable strategy in advanced material development.

## Declaration of generative AI and AI-assisted technologies in the writing process

During the preparation of this work the author(s) used ChatGPT in order to improving readability. After using this tool/service, the author (s) reviewed and edited the content as needed and take(s) full responsibility for the content of the publication

## Funding

The authors acknowledge funding from Australian Research Council (LP180100431, LP210300999, LE190100048, and FT180100232), Taiwan's National Science and Technology Council (113–2119-M-002–001-MBK) and Ministry of Education (112L9006), Nanyang Technological University, and Singapore's National Research Foundation (NRF-NRFF16–2024–0009). The authors thank technical and facility supports from Microscopy Australia, Sydney Nano, and the School of AMME, The University of Sydney.

## CRediT authorship contribution statement

**Chao Huang:** Writing – original draft, Methodology, Investigation, Formal analysis, Data curation. **Chuanjie Cui:** Writing – original draft, Investigation, Formal analysis, Data curation. **Ranming Niu:** Writing – review & editing, Visualization, Supervision, Resources, Project administration, Methodology, Investigation, Funding acquisition, Formal analysis, Data curation. **Fenghua Lu:** Investigation, Formal analysis, Data curation. **Cheng-Yun Wu:** . **Xiaoxiong Zhu:** Resources, Data curation. **Hongzhou Lu:** Supervision, Resources, Investigation, Funding acquisition, Conceptualization. **Yongqing Zhang:** Resources. **Pang-Yu Liu:** Resources, Methodology, Investigation. **Bosheng Dong:** Supervision, Resources, Investigation. **Yi-Hsuan Sun:** Investigation, Data curation. **Hongjian Wang:** Methodology, Investigation, Data curation. **Wei Li:** Supervision, Resources, Project administration, Methodology. **Hung-Wei Yen:** Writing – review & editing, Supervision, Resources, Project administration, Investigation, Funding acquisition. **Aimin Guo:** Supervision, Resources, Project administration, Funding acquisition. **Julie M. Cairney:** Writing – review & editing, Supervision, Resources, Project administration, Funding acquisition. **Emilio Martínez-Pañeda:** Writing – review & editing, Supervision, Resources, Project administration, Methodology, Funding acquisition, Formal analysis, Data curation. **Eason Yi-Sheng Chen:** Writing – review & editing, Validation, Supervision, Resources, Project administration, Methodology, Investigation, Funding acquisition, Conceptualization.

## Declaration of Interest Statement

The authors declare that they have no known competing financial interests or personal relationships that could have appeared to influence the work reported in this paper.

## Acknowledgments

T. Sato, V. Bhatia, A. Indiradevi, L. Stephenson, H.J. Wang, M. Garbrecht, H.W. Liu, J.T. Qu, H.Y. Li and H. Bilal (The University of Sydney) are thanked for their technical supports. E. Y.-S. C. thanks his family.

## Supplementary materials

Supplementary material associated with this article can be found in the online version at doi:10.1016/j.actamat.2025.121231.

## References

[1] H.C. Rogers, Hydrogen embrittlement of metals, Science 159 (1968) 1057–1064.
[2] M.L. Martin, M.J. Connolly, F.W. DelRio, A.J. Slifka, Hydrogen embrittlement in ferritic steels, Appl. Phys. Rev. 7 (2020).
[3] Y.-S. Chen, et al., Hydrogen trapping and embrittlement in metals – A review, Int. J. Hydrog. Energy (2024).
[4] H. Yu, et al., Hydrogen embrittlement as a conspicuous material challenge-comprehensive review and future directions, Chem. Rev. 124 (2024) 6271–6392.
[5] R. Tidball, S. Knoke, Hydrogen and Our Energy Future, DOE/EEA, 2009.
[6] Basic Hydrogen Strategy, The Ministerial Council on Renewable Energy, Hydrog. Relat. Issues (2023).
[7] UK Hydrogen Strategy, Secretary of State for Business, Energy Ind. Strategy (2021).
[8] G. Lovicu, et al., Hydrogen embrittlement of automotive advanced high-strength steels, Metall. Mater. Trans. A 43 (2012) 4075–4087.
[9] H.K.D.H. Bhadeshia, Prevention of hydrogen embrittlement in steels, ISIJ Int. 56 (2016) 24–36.
[10] M. Wetegrove, et al., Preventing hydrogen embrittlement: the role of barrier coatings for the hydrogen economy, Hydrogen 4 (2023) 307–322.
[11] R. Fernández-Sousa, C. Betegón, E. Martínez-Pañeda, Analysis of the influence of microstructural traps on hydrogen assisted fatigue, Acta Mater. 199 (2020) 253–263.
[12] G.M. Pressouyre, Trap theory of Hydrogen embrittlement, Acta Metall. 28 (1980) 895–911.
[13] K. Takai, R. Watanuki, Hydrogen in trapping states innocuous to environmental degradation of high-strength steels, ISIJ Int. 43 (2003) 520–526.
[14] M. Dadfarnia, P. Sofronis, T. Neeraj, Hydrogen interaction with multiple traps: can it be used to mitigate embrittlement? Int. J. Hydrog. Energy 36 (2011) 10141–10148.
[15] R.A. Oriani, The diffusion and trapping of hydrogen in steel, Acta Metall. 18 (1970) 147–157.
[16] K.-i. Ebihara, H. Kaburaki, T. Suzudo, K. Takai, A numerical study on the validity of the local equilibrium hypothesis in modeling hydrogen thermal desorption spectra, ISIJ Int. 49 (2009) 1907–1913.
[17] K. Okuno, K. Takai, Determination of hydrogen diffusibility and embrittlement susceptibility of high-strength steel evaluated at different temperatures based on the local equilibrium theory, Acta Mater. 246 (2023) 118725.
[18] W.Y. Choo, J.Y. Lee, Thermal analysis of trapped hydrogen in pure iron, Metall. Trans. A 13 (1982) 135–140.
[19] F.G. Wei, K. Tsuzaki, Quantitative analysis on hydrogen trapping of TiC particles in steel, Metall. Mater. Trans. A 37 (2006) 331–353.
[20] H.E. Kissinger, Reaction kinetics in differential thermal analysis, Anal. Chem. 29 (1957) 1702–1706.

[21] Y.-S. Chen, et al., Atom probe tomography for the observation of hydrogen in materials: a review, Microsc. Microanal. 29 (2022) 1–15.
[22] M. Koyama, et al., Recent progress in microstructural hydrogen mapping in steels: quantification, kinetic analysis, and multi-scale characterisation, Mater. Sci. Technol. 33 (2017) 1481–1496.
[23] Y.-S. Chen, et al., Observation of hydrogen trapping at dislocations, grain boundaries, and precipitates, Science 367 (2020) 171–175.
[24] J. Takahashi, K. Kawakami, Y. Sakiyama, T. Ohmura, Atomic-scale observation of hydrogen trap sites in bainite–austenite dual-phase steel by APT, Mater. Charact. 178 (2021) 111282.
[25] H. Zhao, et al., Hydrogen trapping and embrittlement in high-strength Al alloys, Nature 602 (2022) 437–441.
[26] Y.-S. Chen et al., Direct observation of individual hydrogen atoms at trapping sites in a ferritic steel. 355, 1196–1199 (2017).
[27] J. Takahashi, K. Kawakami, Y. Kobayashi, Origin of hydrogen trapping site in vanadium carbide precipitation strengthening steel, Acta Mater. 153 (2018) 193–204.
[28] J. Takahashi, K. Kawakami, Y. Kobayashi, T. Tarui, The first direct observation of hydrogen trapping sites in TiC precipitation-hardening steel through atom probe tomography, Scr. Mater. 63 (2010) 261–264.
[29] J. Takahashi, K. Kawakami, T. Tarui, Direct observation of hydrogen-trapping sites in vanadium carbide precipitation steel by atom probe tomography, Scr. Mater. 67 (2012) 213–216.
[30] Z. Zhou, et al., Cryogenic atom probe tomography and its applications: a review, Microstructures 3 (2023) 2023043.
[31] B. Zhang, et al., Improving the hydrogen embrittlement resistance by straining the ferrite /cementite interfaces, Acta Mater. 270 (2024) 119850.
[32] Z.H. Li, et al., Role of deformation on the hydrogen trapping in the pearlitic steel, Scr. Mater. 241 (2024) 115859.
[33] T. Doshida, K. Takai, Dependence of hydrogen-induced lattice defects and hydrogen embrittlement of cold-drawn pearlitic steels on hydrogen trap state, temperature, strain rate and hydrogen content, Acta Mater. 79 (2014) 93–107.
[34] C. Borchers, R. Kirchheim, Cold-drawn pearlitic steel wires, Prog. Mater. Sci. 82 (2016) 405–444.
[35] A. Saksena, et al., Optimizing site-specific specimen preparation for atom probe tomography by using hydrogen for visualizing radiation-induced damage, Int. J. Hydrog. Energy 50 (2024) 165–174.
[36] A. McNabb, P. Foster. (AIME, 1963).
[37] H.E. Kissinger, Variation of peak temperature with heating rate in differential thermal analysis, J. Res. Natl. Bur Stand. 57 (1956) 217–221.
[38] W. Choo, J.Y. Lee, Thermal analysis of trapped hydrogen in pure iron, Metall. Trans. A 13 (1982) 135–140.
[39] Y. He, Y. Li, C. Chen, H. Yu, Diffusion coefficient of hydrogen interstitial atom in α-Fe, γ-Fe and ε-Fe crystals by first-principle calculations, Int. J. Hydrog. Energy 42 (2017) 27438–27445.
[40] S.-H. Yu, H.-B. Jeong, J.-S. Lee, Y.-K. Lee, Micro-axial cracking in unnotched, cold-drawn pearlitic steel wire: mechanism and beneficial effect on the resistance to hydrogen embrittlement, Acta Mater. 225 (2022) 117567.
[41] Y.J. Li, et al., Atomic-scale mechanisms of deformation-induced cementite decomposition in pearlite, Acta Mater. 59 (2011) 3965–3977.
[42] X. Zhang, A. Godfrey, N. Hansen, X. Huang, Hierarchical structures in cold-drawn pearlitic steel wire, Acta Mater. 61 (2013) 4898–4909.
[43] R. Sato, K. Takai, Quantitative hydrogen trap states on high-angle grain boundaries and at dislocations in iron, Scr. Mater. 228 (2023) 115339.
[44] K. Saito, K. Takai, Hydrogen desorption behavior trapped in various microstructures of high-strength steels using thermal desorption analysis, Metall. Mater. Trans. A 52 (2021) 531–543.
[45] M. Nagumo, K. Takai, The predominant role of strain-induced vacancies in hydrogen embrittlement of steels: overview, Acta Mater. 165 (2019) 722–733.
[46] X. Zhang, N. Hansen, A. Godfrey, X. Huang, Structure and strength of sub-100 nm lamellar structures in cold-drawn pearlitic steel wire, Mater. Sci. Technol. 34 (2018) 794–808.
[47] X. Zhang, A. Godfrey, X. Huang, N. Hansen, Q. Liu, Microstructure and strengthening mechanisms in cold-drawn pearlitic steel wire. 59, 3422–3430 (2011).
[48] S. Lynch, Hydrogen embrittlement phenomena and mechanisms, Corros. Rev. 30 (2012) 105–123.
[49] M.C. Jo, et al., Effects of Nb and Mo alloying on resistance to hydrogen embrittlement in 1.9 GPa-grade hot-stamping steels, Mater. Sci. Eng.: A 789 (2020) 139656.
[50] Z.H. Cao, B.N. Zhang, M.X. Huang, Comparing hydrogen embrittlement behaviors of two press hardening steels: 2 GPa vs. 1.5 GPa grade, J. Mater. Sci. Technol. 124 (2022) 109–115.
[51] Y.F. Jiang, W. Xu, Q. Zhang, B. Zhang, Improvement of hydrogen embrittlement resistance by intense pulsed ion beams for a martensitic steel, Int. J. Hydrog. Energy 46 (2021) 21239–21248.
[52] S.-H. Yu, et al., Effects of lamellar structure on tensile properties and resistance to hydrogen embrittlement of pearlitic steel, Acta Mater. 172 (2019) 92–101.
[53] R. Niu, et al., Hydrogen-enhanced deformation in pearlite, Acta Mater. 281 (2024) 120327.
[54] O.C. Hellman, J.B.d. Rivage, D.N. Seidman, Efficient sampling for three-dimensional atom probe microscopy data, Ultramicroscopy 95 (2003) 199–205.
[55] X. Sauvage, J. Copreaux, F. Danoix, D. Blavette, Atomic-scale observation and modelling of cementite dissolution in heavily deformed pearlitic steels, Philos. Mag. A 80 (2000) 781–796.
[56] V.I. Voronin, et al., Composition of cementite in the dependence on the temperature. In situ neutron diffraction study and ab initio calculations, JETP. Lett. 91 (2010) 143–146.
[57] A.H. Cottrell, B.A. Bilby, Dislocation theory of yielding and strain ageing of iron, Proc. Phys. Soc. A 62 (1949) 49.
[58] J. Takahashi, M. Kosaka, K. Kawakami, T. Tarui, Change in carbon state by low-temperature aging in heavily drawn pearlitic steel wires, Acta Mater. 60 (2012) 387–395.
[59] Y. Ivanisenko, W. Lojkowski, R.Z. Valiev, H.J. Fecht, The mechanism of formation of nanostructure and dissolution of cementite in a pearlitic steel during high pressure torsion, Acta Mater. 51 (2003) 5555–5570.
[60] B. Gault, et al., Atom probe tomography, Nat. Rev. Methods Primers. 1 (2021) 51.
[61] J. Takahashi, K. Kawakami, Y. Kobayashi, Quantitative analysis of carbon content in cementite in steel by atom probe tomography, Ultramicroscopy 111 (2011) 1233–1238.
[62] A.J. Breen, et al., Solute hydrogen and deuterium observed at the near atomic scale in high-strength steel, Acta Mater. 188 (2020) 108–120.
[63] H. Suzuki, K. Takai, Summary of round-robin tests for standardizing hydrogen analysis procedures, ISIJ Int. 52 (2012) 174–180.
[64] P.-Y. Liu, et al., Engineering metal-carbide hydrogen traps in steels, Nat. Commun. 15 (2024) 724.
[65] A. McNabb, P.K. Foster, A new analysis of diffusion of hydrogen in iron and ferritic steels, Trans. Metall. Soc. AIME 227 (1963) 618. -&.
[66] E. Legrand, A. Oudriss, C. Savall, J. Bouhattate, X. Feaugas, Towards a better understanding of hydrogen measurements obtained by thermal desorption spectroscopy using FEM modeling, Int. J. Hydrog. Energy 40 (2015) 2871–2881.
[67] A.J. Kumnick, H.H. Johnson, Deep trapping states for hydrogen in deformed iron, Acta Metall. 28 (1980) 33–39.
[68] J.-L. Lee, J.-Y. Lee, Hydrogen retrapping after thermal charging of hydrogen in iron single crystal, Metall. Trans. A 20 (1989) 1793–1802.